Structural and magnetic study of Tb³⁺ doped zinc ferrite by sol-gel auto-combustion technique

Shrinivas G. Jamdade[1], Popat S. Tambade[2], Sopan M. Rathod[3]

[1]Department of Physics, Nowrosjee Wadia College, Pune, India
[2]Department of Physics, Prof. Ramkrishna More Arts, Commerce and Science College, Akurdi, Pune, India
[3]Department of Physics, Abasaheb Garware College, Pune, India

Corresponding author: Shrinivas G. Jamdade, hv_jamdade@yahoo.com

ABSTRACT In this study, the influence of Tb^{3+} substitution in zinc ferrite is reported. $ZnTb_xFe_{(2-x)}O_4$ ($x = 0$, 0.025, 0.05, 0.075, 0.1, 0.125, and 0.15) were prepared using sol-gel auto-combustion technique. All the samples were sintered at 400 °C for 4 hours. The structure has been studied using XRD, FTIR, UV-visible, and VSM. X-ray diffraction evaluation demonstrates formation of spinel ferrite with nano size distribution. Vibrating sample magnetometer was used to study the magnetic properties of the samples. It was found that as terbium content increases, the coercive field decreases while the saturation magnetization increases. The Tb^{3+} doped nano-crystalline zinc ferrites show ferrimagnetic behavior. FTIR analysis show the presence of two expected bands attributed to tetrahedral and octahedral metal oxygen vibrations at 320 and 450 cm^{-1}.

KEYWORDS sol-gel auto-combustion technique, zinc ferrite, terbium additive, cubic spinel structure, nano structure

FOR CITATION Jamdade S.G., Tambade P.S., Rathod S.M. Structural and magnetic study of Tb³⁺ doped zinc ferrite by sol-gel auto-combustion technique. *Nanosystems: Phys. Chem. Math.*, 2023, **14** (2), 254–263.

1. Introduction

Nano crystalline spinel ferrites were studied by many researchers in recent years. The most common formula for the spinel ferrite is given as AB_2O_4 where A^{2+} ions occupy tetrahedral with B^{3+} ions at the octahedral sites. Cation distribution in the tetrahedral and octahedral sites changes the properties of spinel ferrites. It has been studied that the properties of ferrites were changed with the help of the doping and substitution of a foreign ion, and introduction of a metal cation with higher electronegativity. Rare-earth elements (RE) are commonly used additives for improving the spinel ferrite properties [1, 2]. In case of spinel ferrites, the conduction mechanism and magnetic properties are mostly due to the spin coupling of 3d electrons which arises from the Fe–Fe interaction. But, when spinel ferrite Fe^{3+} ions are partially replaced by rare-earth ions of 4f elements, the RE–FE interaction appears and results in 3d–4f coupling. This 3d–4f coupling in ferrites results in variation in the electric and magnetic properties due to the orbital nature of the unpaired 4f electrons of RE ions [3, 4].

Among various spinel ferrites, zinc ferrite has a wide range of applications such as photoconductive materials, information storage, sensors, electronic devices, and in high frequency applications. $ZnFe_2O_4$ magnetization studies show the presence of a paramagnetic phase at room temperature and a weak anti-ferromagnetic property below its Neel temperature [5–7]. Recent studies on nano-crystalline $ZnFe_2O_4$ ferrite also mentioned the presence of ferrimagnetic ordering at room temperature. These changes in magnetic ordering are owing to the cation's redistribution between tetrahedral and octahedral sites. Thus, the properties shown by $ZnFe_2O_4$ ferrites are changed with the crystallite size and inversion of cations on the sites [8–10].

Various methods were developed to have different nano-crystalline $ZnFe_2O_4$ spinel ferrites like microwave based hydrothermal, decomposition of double layered hydroxide precursor, hydrothermal synthesis, urea combustion, reverse micelle method, dip-coating, solvo-thermal analysis, and co-precipitation [11–14]. The sol-gel auto combustion method is preferred because of its high degree of compositional homogeneity, low processing temperature, and low cost [15–21]. In the present study, the aim is to see the influence of rare-earth ion Tb^{3+} on structural and magnetic properties of Zn ferrites. $ZnTb_xFe_{(2-x)}O_4$ nano ferrite is synthesized by sol-gel auto combustion method followed by its heat treatment and then its characterization is done by XRD, UV-visible, FTIR, and VSM tools. One can find several papers concerning to different properties of doped nano-crystalline zinc ferrites [23–25].

2. Synthesis details

Terbium substituted zinc nano crystalline ferrite ($ZnTb_xFe_{(2-x)}O_4$) (x = 0, 0.025, 0.05, 0.075, 0.1, 0.125, and 0.15 represented by JX1, JX2, JX3, JX4, JX5, JX6, and JX7, respectively, in all figures) were prepared by sol-gel auto-combustion method. The high purity AR grade ferrite nitrate (($Fe(NO_3)_2) \cdot 9H_2O$), zinc nitrate (($Zn(NO_3)_2) \cdot 6H_2O$), terbium nitrate (($Tb(NO_3)_2) \cdot 5H_2O$), ammonium hydroxide solution (NH_4OH) were used. The citric acid ($C_6H_8O_7, H_2O$) was used as a fuel. The nitrates and citric acid in stochiometric proportion are dissolved in 100 ml distilled water, which is stirred till homogenous solution is obtained. Drop by drop ammonium hydroxide solution is added to maintain pH = 7 during the stirring process. Then the mixed solution was kept on hot plate at 80 °C for 2 to 3 hours to obtain the sol of it. After half an hour this sol becomes a viscous gel. Then, we get fine powder of ferrite nanoparticles after auto-combustion happens. The powder was sintered at 400 °C for 4 hours in the muffle furnace.

3. Results and discussion

3.1. X-ray diffraction (XRD) analysis

XRD analysis of prepared $ZnTb_xFe_{(2-x)}O_4$, where JX1 is x = 0, JX2 is x = 0.025, JX3 is x = 0.05, JX4 is x = 0.075, JX5 is x = 0.1, JX6 is x = 0.125, and JX7 is x = 0.15 nano-particles sintered at 400 °C for 4 hours, were performed using X-ray diffractometer with CuKα radiation of wavelength 1.5405 Å. XRD Fig. 1 for pure and terbium doped zinc ferrite powder sample shows six major diffractions peaks in the range of 2θ equal to 29 – 30, 35 – 36, 42 – 43, 53 – 54, 56 – 57, and 62 – 63 corresponding to planes (220), (311), (400), (422), (511), and (440), respectively. These peaks are found to be associated with cubic spinel structure (JCPDS card number 22-1012). The robust reflection comes from the (311) plane denoting the spinel structure. The moderate peak intensity indicates low degree of crystallinity of prepared ferrite samples while the broadening of peaks indicates the nanometer size of the crystallite. Many researchers have mentioned orthorhombic phase ($TbFeO_3$) formation in the rare-earth doped ferrites even at a low doping concentration. In our case, we observed the secondary phase as a small reflection peak at $2\theta = 31.78°$ as $TbFeO_3$ phase while Fe_2O_3 phase is seen at $2\theta = 36.66°$ for the reflection plane (121) and (110), respectively [2].
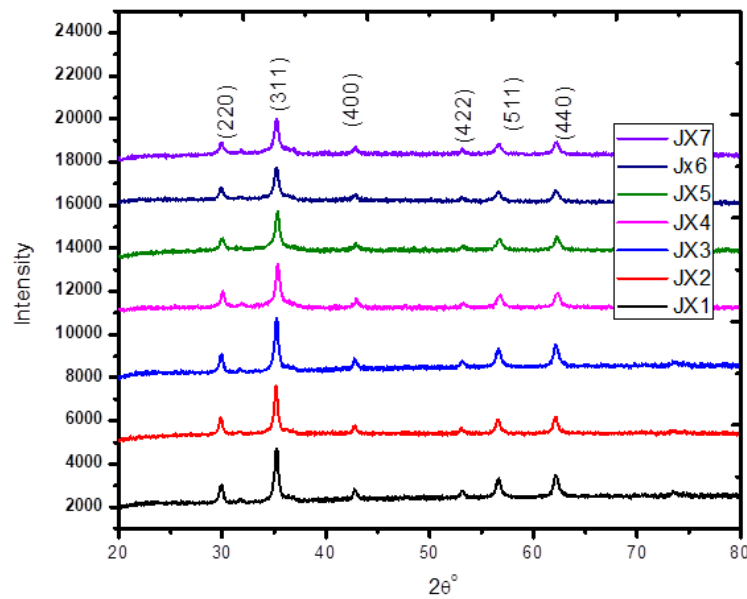

FIG. 1. XRD pattern of $ZnTb_xFe_{(2-x)}O_4$ powder

Using XRD data, lattice constant values of ferrite samples were calculated by Bragg's equation

$$a = d \cdot \sqrt{h^2 + k^2 + l^2}, \tag{1}$$

where d is interplanar distance and h, k, l are the miller indices. Normally the lattice constant value increases with addition of rare-earth doping owing to the difference in radii of rare-earth ions and Fe^{3+} ions. However, a slight decrease is observed for the sample JX4 with x = 0.075. This suggests the possibility of some Tb^{3+} ions occupying the tetrahedral sites up to this terbium concentration, which results in the contraction of the unit cell. For $x > 0.075$, lattice constant is increasing owing to the expansion of the unit cell caused by the Tb^{3+} substitution. As the Tb^{3+} ions, having large ionic radii (0.923 Å), enters into the octahedral (B) site in place of Fe^{3+} ions having smaller radii (0.67 Å) results into internal stress to make the lattice distorted and unit cell expansion. Similar results have been reported by many researchers, this is attributed to the nonlinear variation of lattice constant owing to the distribution of cations at A and B sites [3].

The crystallite size was calculated using Debye–Scherrer formula,

$$D = 0.89 \cdot \frac{\lambda}{\beta \cos \theta}. \tag{2}$$

The crystallite size was calculated for all the compositions using the high intensity (311) peak. The obtained crystallite size of the samples is within the nano region. The crystal size varies from 5 to 7 nm. The preparation condition followed here probably gives rise to different rates of ferrite formation for different concentrations of Tb^{3+} favouring the variation in crystallite size. The crystallite size was observed to increase up to $x = 0.05$ by increasing Tb^{3+} concentration. Thereafter crystallite size is found to decrease with terbium content. Excess of Tb^{3+} ions on or near the grain boundaries which impedes the grain boundary mobility may be the reason for this decrease. The average crystallite size (D) and lattice strain (ε) also was calculated using Williamson–Hall (W-H) equation which is given as

$$\frac{\beta \cos \theta}{\lambda} = \frac{1}{D} + \frac{\varepsilon \sin \theta}{\lambda}. \tag{3}$$

Here ε is the lattice strain, D is the crystallite size, λ is the wavelength of X-ray used, β is the Full Width at Half Maximum and θ is Bragg's angle. From above equation (3) the plot of $\beta \cos \theta$ versus $\sin \theta$ will be in the form of a straight-line equation giving the slope as lattice strain and from the intercept we can calculate the crystallite size. Non-zero slopes of the W-H plot are indicative of inhomogeneous (strained) growth of the unit cells. These values are in good agreement with the value obtained from the Debye–Scherrer formula. The crystallite size obtained from Debye–Scherrer's formula and W-H plot are tabulated in Table 1. The uncertainties in all values mentioned in Table 1 are ± 0.5 %.

In the present case, the lattice strain was seen to decrease with Tb^{3+} doping up to $x = 0.05$ and then increases for $x \geq 0.05$. The variation in lattice strain parameter also may be due to presence of impurity phases and incomplete replacement of Fe^{3+} cations by Tb^{3+} cations. The dislocation density is given as $\rho_d = 1/D^2$, where D is the crystallite size of the sample. In the present case, the dislocation density increases up to $x = 0.1$ except $x = 0.05$ and then reduces with Tb^{3+} ion concentration as the crystallite size of all the samples is small [3, 4]. Thus, the size of nano crystals (D) and the lattice parameter (a) non monotonically increases while the lattice strain and the dislocation density non-linearly decrease with doping of Tb^{3+} in the Zinc ferrite sample.

X-ray density were calculated using the equation

$$\delta_s = \frac{8M}{Na^3}. \tag{4}$$

Here 8 represents the number of atoms in the unit cell of the spinel lattice, M is the molecular weight of TbZn ferrite samples, N is Avogadro number, and a is lattice constant. The values of X-ray density of the synthesized sample vary from 5.3189 to 5.688 g/cm^3 (Fig. 2). The increase in X-ray density of samples is due to increase in the molar mass of the doped Tb^{3+} ions (158.92 g/mole) as compared to Fe^{3+} (55.84 g/mole), and Zn^{2+} (65.41 g/mole) ion. Fig. 2 depicts the change in the value of X-ray density with terbium substitution.

The distance between magnetic ions (hopping length) in site A (tetrahedral) and B site (octahedral) where calculated by using the following relations

$$L_A = M_A - M_A = \left(\frac{\sqrt{3}}{4} \right) a, \tag{5}$$

$$L_B = M_B - M_B = \left(\frac{\sqrt{2}}{4} \right) a, \tag{6}$$

$$L_{AB} = M_A - M_B = \left(\frac{\sqrt{\pi}}{4} \right) a, \tag{7}$$

where a is the lattice constant.

The determination of the inter-atomic distance is an amenable method to give one a description of the crystallographic structure and the magnetic properties, where M_A and M_B refer to the cations at the center of the tetrahedral (A) and octahedral (B) sites, respectively [5]. The variations in the hopping length for tetrahedral site (L_A) and octahedral site (L_B) were shown in Fig. 2. It is clear that the distance between the magnetic ions increases as the Tb^{3+} content increases except for JX3, $x = 0.1$ sample.

3.2. UV-visible spectroscopy analysis

Figure 3 illustrates the DRS (absorption mode) optical absorption spectra for $ZnTb_xFe_{(2-x)}O_4$ ($x = 0$, 0.025, 0.05, 0.075, 0.1, 0.125, and 0.15) nanoparticles in the UV-visible range for the prepared samples at room temperature sintered at 400 °C. There are three bands of absorption found at 280, 350 and 420 nm in correlation with the XRD conclusion. This absorption builds upon the constitution and measure of heat content of the test samples as given in the Figs. 3 and 4.

Three kinds of electronic shifts take place in the optical absorption of Fe^{3+} samples. As is disclosed from Fig. 3 that for $x = 0.1$ composition sample, the electronic transition for charge carries over lies in the wavelength range of 450
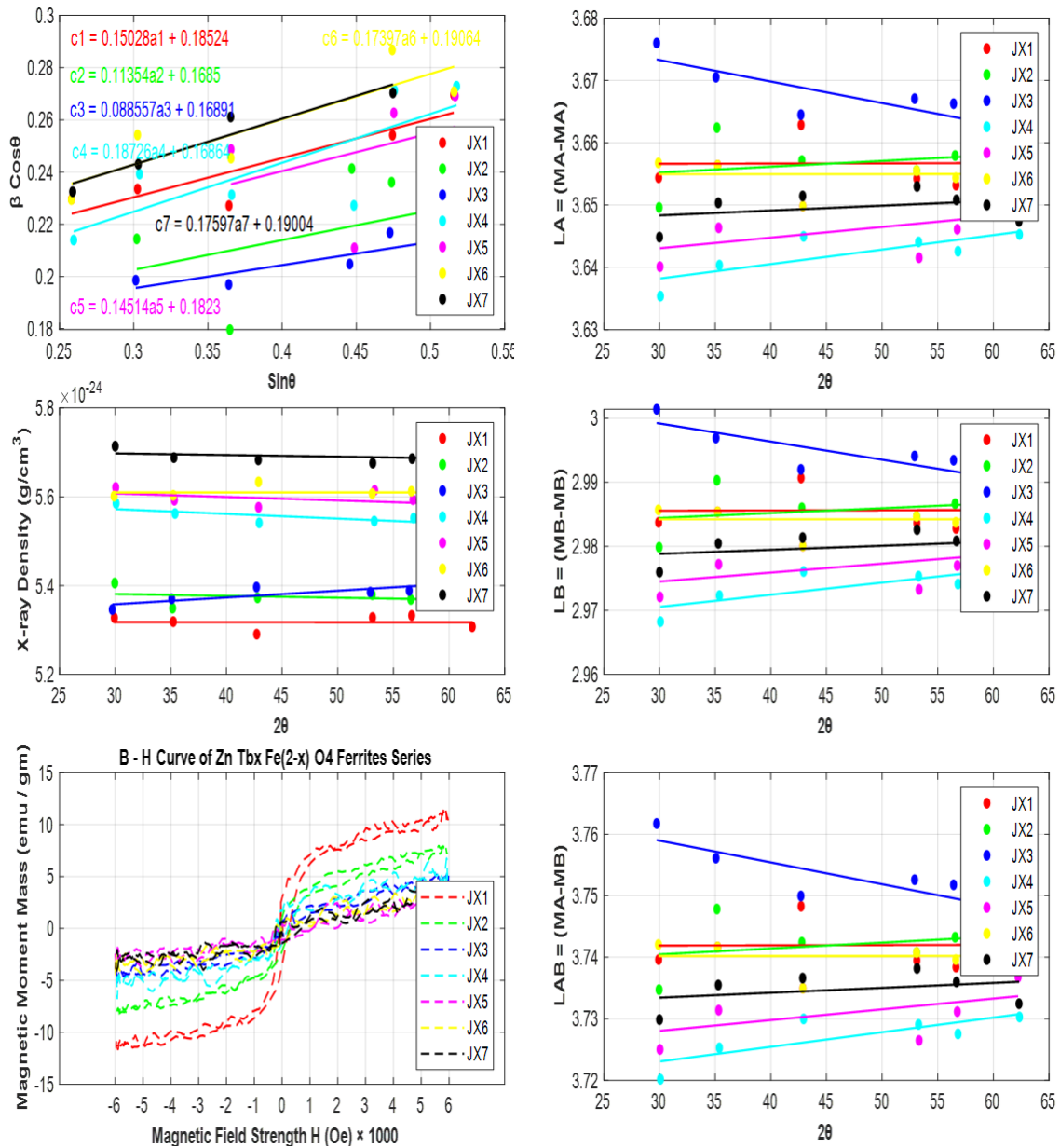
FIG. 2. W-H Plots, X-ray Density verses 2θ, M–H loops, LA verses 2θ, LB verses 2θ, and LAB verses 2θ for $ZnTb_xFe_{(2-x)}O_4$ powder

to 500 nm which is in the optical region while the ligand field change over occurs in the interval of wavelength 750 to 780 nm also in the optical region.

The band gap energy is calculated using the formula

$$E = h\gamma = \frac{hc}{\lambda}. \tag{8}$$

The band gap energy decreases from 2.579 to 2.103 eV for the samples which are sintered at 400 °C. The outcome shows that composition and annealing measure of the heat contained in the samples put a major impact on the optical characteristics [6–8].

3.3. FTIR analysis

The FTIR spectra of the investigated $ZnTb_xFe_{(2-x)}O_4$ samples are shown in Fig. 5. In the wave number range of 1600 to 200 cm^{-1} two main metal oxygen bands are seen in the infrared spectra of spinel ferrites The higher band γ_1, generally observed in the range of 520 to 530 cm^{-1}, is caused by the stretching vibrations of the tetrahedral metal oxygen bond and the lowest band γ_2, usually observed in the range 400 to 420 cm^{-1}, is caused by metal oxygen vibration in the octahedral sites. IR absorption bands mainly appear owing to the oxygen ions vibrations with cations at different
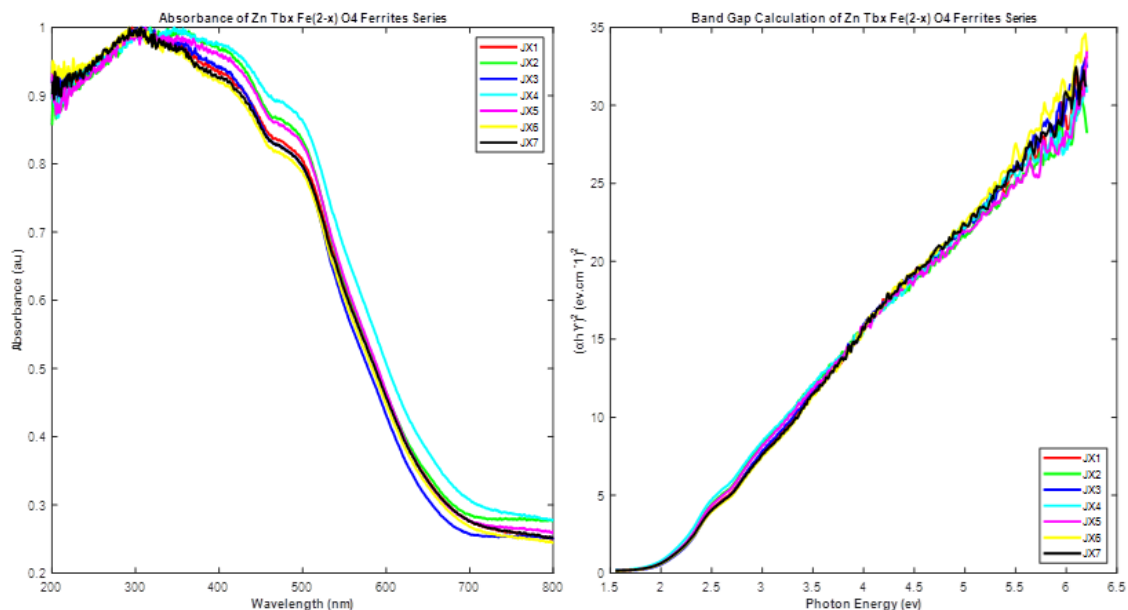
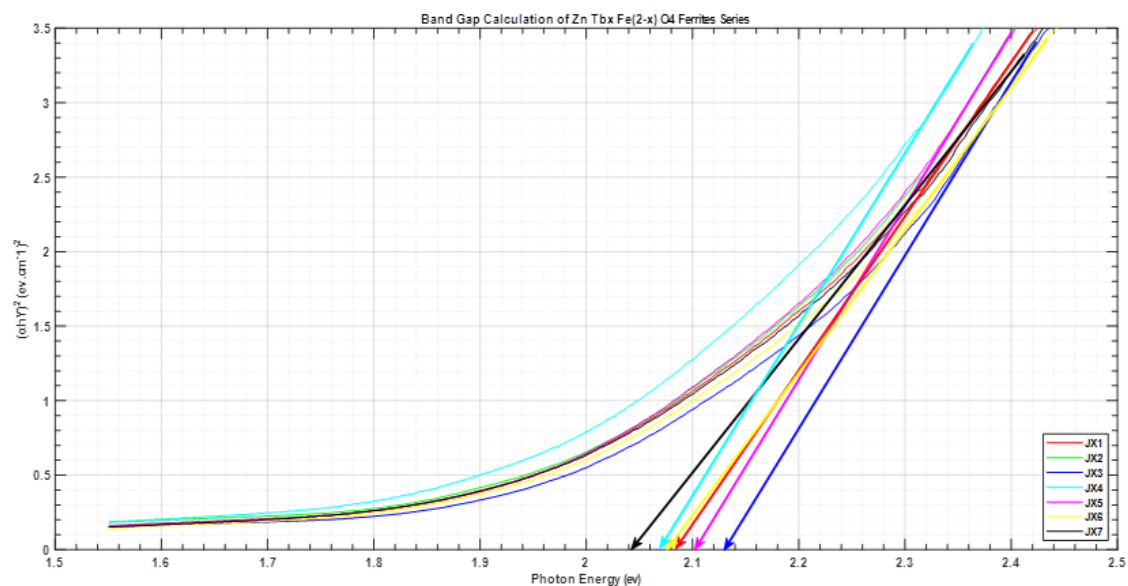FIG. 3. Absorbance spectra, and $(\alpha h\gamma)^2$ versus photon energy $(h\gamma)$ for $ZnTb_xFe_{(2-x)}O_4$ powder

FIG. 4. $(\alpha h\gamma)^2$ versus photon energy $(h\gamma)$ for $ZnTb_xFe_{(2-x)}O_4$ powder

frequencies. But the spinel structure exhibits two IR vibrational bands at $\gamma_1 = 546.86$ cm^{-1} and at $\gamma_2 = 449.42$ cm^{-1} corresponding to familiar intrinsic vibrations of tetrahedral site and octahedral site.

The vibrational frequencies of the IR bands γ_1 and γ_2 are such that the values of γ_1 slightly increase but γ_2 shifts to the lower frequency side with the increase of terbium content. It is known that increase in the site radius reduces the fundamental frequency and therefore the centered frequency should shift towards the lower frequency side. The shift in γ_1 may be due to the perturbation occurring in the Fe^{3+}–O^{2-} bonds by the substitution of Tb^{3+} ions. Increase in site radius may be expected due to the replacement of smaller Fe^{3+} ions by larger Tb^{3+} ions in the octahedral sites. Decrease in γ_2 and increase in γ_1 observed for the sample with $x = 0.1$ may be due to the formation of $TbFeO_3$ phase [9–11].

3.4. VSM analysis

Figure 2 shows magnetic hysteresis loop of samples at room temperature. The saturation magnetization (M_S), co-ercivity (H_c), and magnetic remanence (M_r) of all the samples are given in Table 2. It is clear from the value that MS is decreasing with increase in Tb^{3+} concentration owing to large Tb^{3+} ion radii (0.93 Å) than ionic radii of Fe^{3+} ions (0.695 Å) preferably occupying octahedral (B sites). The magnetic moments of rare-earth ions generally originate from
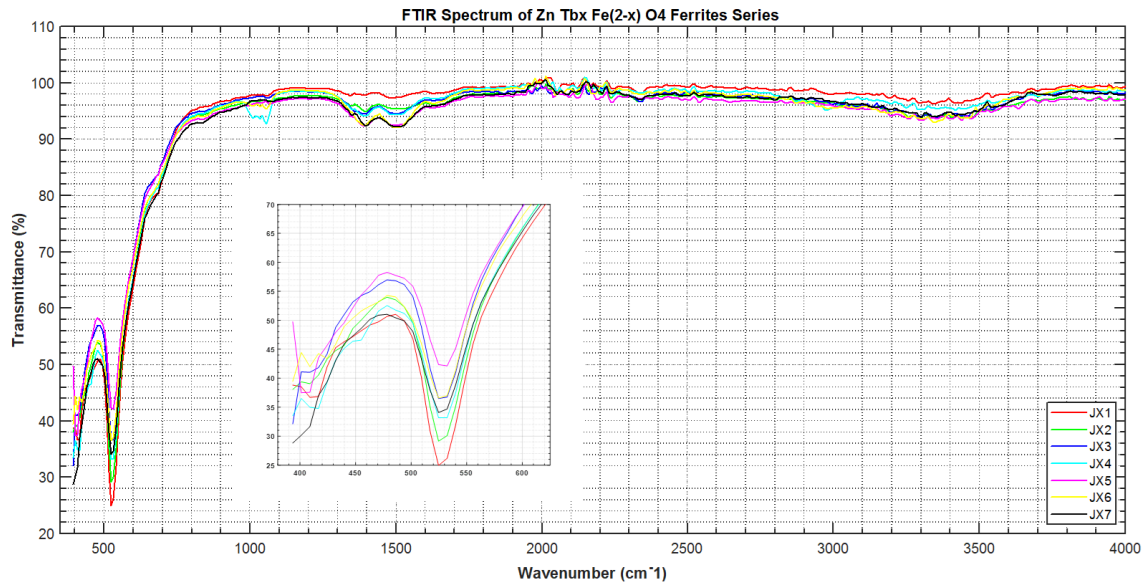
FIG. 5. FTIR spectra for $\text{ZnTb}_x\text{Fe}_{(2-x)}\text{O}_4$ powder

localized 4f electrons and these are characterized by lower magnetic ordering temperatures. Therefore, their magnetic dipolar orientations exhibit disordered form at room temperature and hence are paramagnetic and contribute very little to the magnetization of doped ferrites at room temperature. As the terbium concentration increases, B sub-lattice magnetization decreases. Further substitution of Fe^{3+} magnetic ions by paramagnetic Tb^{3+} ions in B site deteriorates AB super-exchange interaction. Thus, the ferrimagnetic ordering of Zn ferrite is disturbed by the addition of Tb^{3+} ions and hence M_S decreases.

The high magnetization at low doping is attributed to the ratio of Fe^{3+} to Fe^{2+} being maximum at $x = 0$ composition. The saturation magnetization monotonically decreases with increasing Tb^{3+} concentration. Value of saturation magnetization depends on grain size and preparation temperature. The decrease in saturation magnetization is owing to the magnetic disorder on B sites caused by the presence of paramagnetic terbium ion on B site. It has been observed that the spin canting is caused by the doping of rare earth ions. Since Tb is a rare earth metal ion, and it causes the transformation of co-linear ferrimagnetic order into non-colinear arrangement of spins on B sites, hence saturation magnetization is reduced. Also, no more Fe^{3+} ions are transferred to the octahedral sites which lead to the decrease of saturation magnetization. The decrease of saturation magnetization for higher concentration of Tb^{3+} ions may also be attributed to the secondary TbFeO$_3$ phase which has a low value of magnetization.

The coercivity value slowly increases with increase of Tb^{3+} content till it reaches maximum value at $x = 0.1$ composition and then decreases. The increase in coercivity at $x = 0.1$ may be attributed to an enhancement of the magneto crystalline anisotropy and reduction in the grain size. The coercivity is enhanced due to reduction of particle size until single domain particles are reached and then decreases as the super paramagnetic limit is approached. For $x \geq 0.1$, the coercivity decreases which may be due to the decrease in the magnetic anisotropy. The large and small grains would reduce the coercivity due to the emergence of super para-magnetism. The magnetic anisotropy is the accumulative contribution of cations in A site and B site. Therefore, magnetic LS coupling at lattice sites is directly related to the magnetic property such as super para-magnetism. The increase in coercivity may also be related to the appearance of secondary phases TbFeO$_3$ on or near the grain boundaries which impede the motion of domain walls.

The reduction in M_r may be explained on the basis of magnetic dilution. The Zn ion is a divalent cation while terbium is trivalent, when a divalent ion replaced by a trivalent ion then some of the Fe^{3+} ions are converted to Fe^{2+} ions to maintain the electro-neutrality which results in the reduction of magnetic moment as Fe^{3+} has magnetic moment of $5\mu_B$ while that of Fe^{2+} has $4\mu_B$. The super exchange interaction decreases as Fe^{2+}–O^{2-}–Fe^{3+} exchange interaction is weaker than Fe^{2+}–O^{2-}–Fe^{3+} which is responsible for the reduction in M_r.

The saturation magnetization (M_S), coercivity (H_c), remanence (M_r) and Statured Magnetic Field (H_M) values are found to be in the range of 10.53 – 3.39 emu/g, 0.20 – 1.09 Oe, 2.95 – 0.30 emu/g, and 5.985 – 5.90 Oe, respectively. These values demonstrate the ultra-soft ferrimagnetic nature of different ZnTb$_x$Fe$_{(2-x)}$O$_4$ ferrites at room temperature. The values of the magnetic parameters are given in Table 2. The uncertainties in all values mentioned in Table 2 are ± 0.05 %.

TABLE 1. Diffraction Angle (2θ), d Interplaner Spacing (d), Full Width at Half Maxima (β), Lattice Constants (a), Volume of Cell (V_{cell}), X-ray Density (DX), Crystallite Size (D), and Bandgap (eV) with substitution for $ZnTbxFe_{(2-x)}O_4$

x	2θ	d	FWHM (β)	Lattice Parameter (a) Å	V_{cell} (Å³)	X-ray Density (DX) in gmcm⁻³	D (nm) (DS Method)	D (nm) (WH Method)	Strain (ε) D-S Method	Strain (ε) W-H Method	Dislocation Density (δ)	Bandgap (eV)
0	35.22	2.5460	0.2450	8.4440	602.0727	5.319	5.871	5.3984	0.1587	0.15028	0.03010	2.08
0.025	35.16	2.5502	0.2249	8.4580	605.0623	5.349	6.395	5.9347	0.1503	0.11354	0.03010	2.1
0.05	35.08	2.5558	0.2082	8.4767	609.0801	5.370	6.905	5.9203	0.1391	0.08855	0.02265	2.103
0.075	35.38	2.5348	0.2511	8.4071	594.1984	5.562	5.731	5.92979	0.1603	0.18726	0.03158	2.065
0.1	35.32	2.5390	0.2714	8.4209	597.1347	5.592	5.302	5.48546	0.1673	0.14514	0.03315	2.1
0.125	35.22	2.5460	0.2667	8.4440	602.0727	5.603	5.393	5.24548	0.1655	0.17397	0.03298	2.08
0.15	35.28	2.5418	0.2550	8.4301	599.1032	5.688	5.642	5.2620	0.1577	0.17597	0.02984	2.04

TABLE 2. Summary of Coercivity (H_C), Saturation Magnetization (M_S), Retentivity (M_r), Squareness Ratio (S_R), Statured Magnetic Field (H_M), μ peak (Peak Relative Permeability), Molecular Weight of Composition, Magneton Number n_B (Calculated), Magneton Number n_B (Observed), and Anisotropic Constant (K) with substitution for $ZnTb_xFe_{(2-x)}O_4$.

x	H_C (Oe)	M_S (emu/g)	M_r (emu/g)	S_R (M_r/M_S)	H_M	μ peak (Peak Relative Permeability)	Molecular Weight of Composition	Magneton Number n_B (Calculated)	Magneton Number n_B (Observed)	Anisotropic Constant
0	0.25	10.533	2.95	0.280072	5.967	1404.70847	241.066	0.454637	0.671039	2.7429688
0.025	0.3	7.1799	1.1	0.153205	5.925	964.31783	243.646	0.313223	0.671055	2.2437188
0.05	0.3	5.1389	0.65	0.126486	5.985	683.27600	246.223	0.226556	0.673039	1.6059063
0.075	0.2	6.032	1.7	0.281830	5.93	809.46261	248.8008	0.268713	0.668366	1.2566667
0.1	1.09	3.392	0.4	0.117924	5.9	457.50304	251.3778	0.152672	0.669066	3.8513333
0.125	0.41	3.76	0.3	0.079787	5.96	502.03239	253.9558	0.170971	0.670724	1.6058333
0.15	0.69	3.44	0.6	0.174418	5.976	458.07649	256.5315	0.158006	0.669748	2.4725

The experimental magnetic moment (n_B) (observed) was calculated using the relation

$$n_B = \frac{MM_S}{5585}.$$ (9)

Table 2 shows n_B values. The squareness ratio, $R = M_r/M_S$, for all the samples were calculated from M_S and M_r data which indicates ferrimagnetic behavior of synthesized samples. Usually, the nanoparticles are considered to be in the multi-magnetic domain for $R \geq 0.5$ and in single magnetic domain when $R < 0.5$. Thus, all nanoparticles are within a single magnetic domain. It is worth noting that squareness ratio values are below than 0.5 signify the presence of strong surface spin disordering.

3.5. SEM analysis

Scanning electron microscopy was done to reveal the microstructure of ferrite and the morphology of the nanoparticles. The SEM images (Fig. 6) show a non-uniform particle distribution. All the samples show agglomeration of particles with nearly spherical kind of morphology. The agglomeration of the particles leads to the present structure. It is due to the effect of reaction time and sintering temperature.
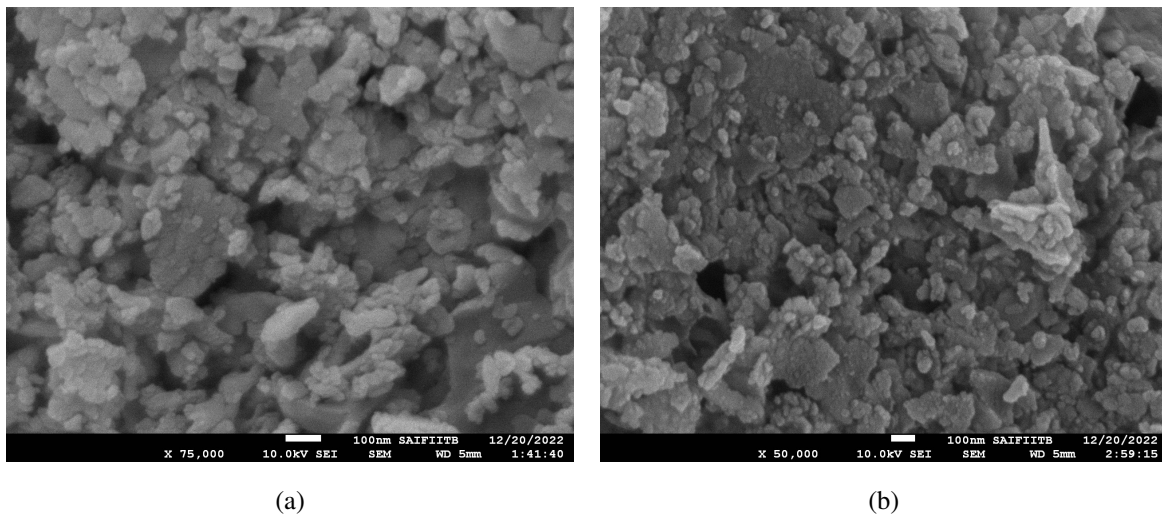

(a)   (b)

FIG. 6. SEM images of $\mathrm{ZnTb}_x\mathrm{Fe}_{(2-x)}\mathrm{O}_4$ powder for $x = 0.025$ (a) and 0.075 (b)

3.6. EDX analysis

EDX has been performed in order to study the composition of the samples. EDX study exhibits the elemental percentage of each element expected to be present in the ferrite sample. The height of the peaks in the EDX graphs (Fig. 7) represents the proportion of each element in the finally sintered ferrite sample. With the increase of Tb concentration, the graph exhibits an increase in height of the Tb peaks. The atomic ratio of Zn:Tb:Fe is about 1:1:4 indicating that the chemical formula of the prepared specimen is consistent with the experimental stoichiometry. Also, all the elements are seen to be present in their respective compositions (Table 3). Terbium concentration was found to be in the grain boundary rather than that in grains. This indicates low solubility of terbium in the spinel structures. This indicates that only a small amount of terbium may be actually getting substituted inside the spinel lattice.

TABLE 3. Elementwise weight % and atomic % of different composition of $\mathrm{ZnTb}_x\mathrm{Fe}_{2-x}\mathrm{O}_4$ ferrite

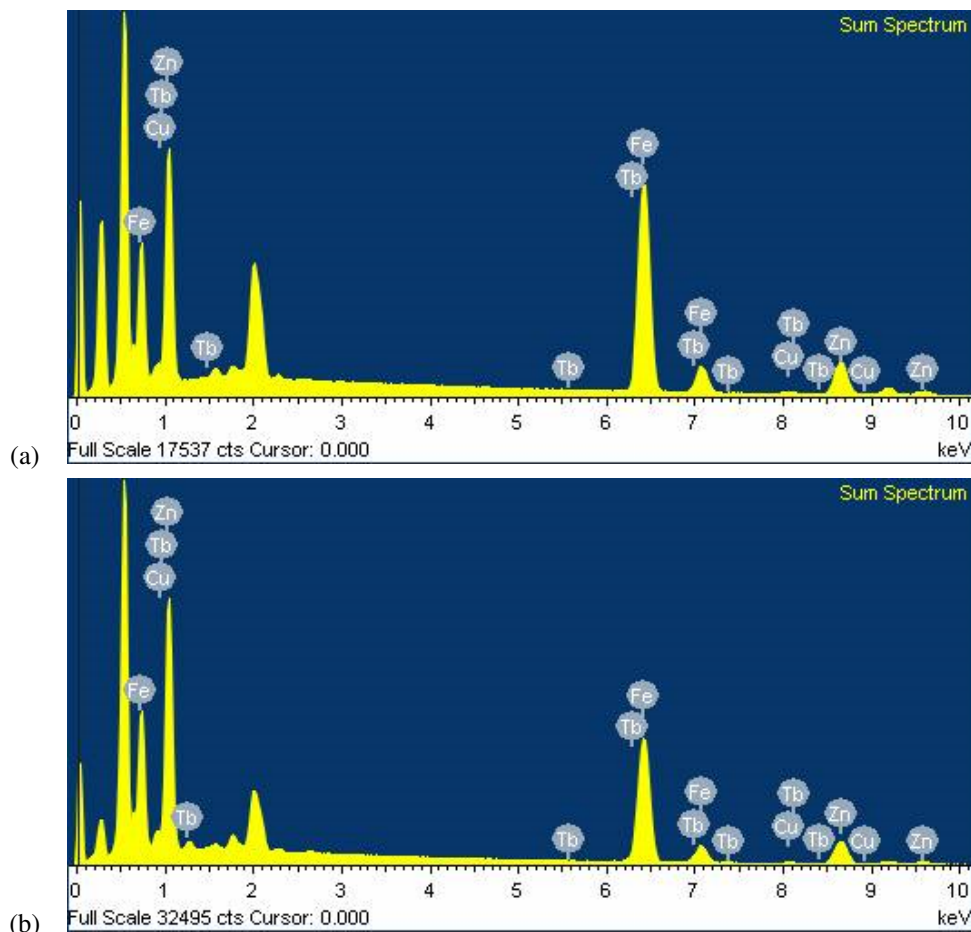| Element	Weight %	Weight %	Weight %	Atomic %	Atomic %	Atomic %
x	0.0	0.05	0.125	0.0	0.05	0.125
Fe K	65.29	52.23	51.85	69	57.52	58.98
Zn L	34.05	43.32	38.05	30.75	40.76	36.98
Tb L	0.66	4.45	10.11	0.24	1.72	4.04

FIG. 7. EDX images of $ZnTb_xFe_{(2-x)}O_4$ powder for $x = 0.025$ (a) and 0.075 (b)

4. Conclusion

Fine particles of $ZnTb_xFe_{(2-x)}O_4$ were prepared by sol-gel auto-combustion technique. The particle size steadily increases with increase in terbium content. The crystallite size lies in the range of 5 to 7 nm. XRD shows partial immersion of Tb^{3+} ions in the spinel lattice and other ions are reversed into secondary phases on grain boundaries. Structural distortions are seen in the lattice. It is revealed that with an increase in terbium amount, the coercive field decreases significantly after maximum value while the saturation magnetization and permanent magnetization also decreases. This may be due to particle size effect, magnetic dilution, spin canting phenomena, and hence reduction of super exchange interaction. The results revealed that terbium cation could reduce magneto crystalline anisotropy of zinc ferrite and consequently altered the magnetic phase to a soft one.

References

[1] Hu J.Y., Liu X.S., Kan X.C., Feng S.J., Liu C.C., Wang W., Rehman K.M.U., Shazed M., Zhou S.Q., Wu Q.Y. Characterization of texture and magnetic properties of $Ni_{0.5}Zn_{0.5}Ti_xFe_{2-x}O_4$ spinel ferrites. *J. Magn. Magn. Mater.*, 2019, **489**, 165411.

[2] Li L.Z., Zhong X.X., Wang R., Tu X.Q., Peng L. Structural and magnetic properties of Co-substituted NiCu ferrite nanopowders. *J. Magn. Magn. Mater.*, 2017, **433**, P. 98–103.

[3] Kokare M.K., Jadhav N.A., Kumar Y., Jadhav K.M., Rathod S.M. Effect of Nd^{3+} doping on structural and magnetic properties of $Ni_{0.5}Co_{0.5}Fe_2O_4$ nanocrystalline ferrites synthesized by sol-gel auto combustion method. *J. of Alloys and Compounds*, 2018, **748**, P. 1053–1061.

[4] Kokare M.K., Jadhav N.A., Singh V., Rathod S.M. Effect of Sm^{3+} substitution on the structural and magnetic properties of NiCo nanoferrites. *Optics and Laser Technology*, 2019, **112**, P. 107–116.

[5] Gao Y., Wang Z., Pei J.J., Zhang H.M. Structure and magnetic properties correlated with cation distribution of $Ni_{0.5-x}Mo_xZn_{0.5}Fe_2O_4$ ferrites prepared by sol-gel auto-combustion method. *Ceram. Int.*, 2018, **44**, P. 20148–20153.

[6] Rekorajska A., Cichowicz G., Cyranski M.K., Grden M., Pekala M., Blanchard G.J., Krysinski P. Synthesis and Characterization of Tb-Doped Nanoferrites. *Chem. Nano Mat.*, 2018, **4**, P. 231–242.

[7] Rehman A.U., Morley N.A., Amin N., Arshad M.I., Nabi M.A., Mahmood K., Iqbal F. Controllable synthesis of La^{3+} doped $Zn_{0.5}Co_{0.25}Cu_{0.25}Fe_{2-x}La_xO_4$ ($x = 0.0, 0.0125, 0.025, 0.0375, 0.05$) nano-ferrites by sol-gel auto-combustion route. *Ceram. Int.*, 2020, **46** (18A), P. 29297–29308.

[8] Awati V., Badave K., Bobade D. Effect of Tb^{3+} substitution on structural, optical and magnetic properties of $NiCuZnFe_2O_4$ prepared by sol-gel route. *Indian J. of Physics*, 2022, **96** (1), P. 89–101.

[9] Bulai G., Diamandescu L., Dumitru I., Gurlui S., Feder M., Caltun O.F. Effect of rare earth substitution in cobalt ferrite bulk materials. *J. Magn. Magn. Mater.*, 2015, **390**, P. 123–131.

[10] Hussain K., Amin N., Arshad M.I. Evaluation of structural, optical, dielectric, electrical, and magnetic properties of Ce^{3+} doped $Cu_{0.5}Cd_{0.25}Co_{0.25}Fe_{2-x}O_4$ spinel nano-ferrites. *Ceram. Int.*, 2021, **47**, P. 3401–3410.

[11] Kumar K.V. Tunable optical bandgap of gadolinium substituted nickel-zinc ferrite nanoparticles-effect of calcination temperature on its optical parameters. *Advances in Materials Physics and Chemistry*, 2022, **12**, P. 33–45.

[12] Rathod S.M., Deonikar V.G., Mirage P.P. Synthesis of Nano-Sized Cerium Doped Copper Ferrite, Their Magnetic and Optical Studies. *Adv. Sci. Lett.*, 2016, **22**, P. 964–966.

[13] Ghodake J.S., Kambale R.C., Shinde T.J., Maskar P.K., Suryavanshi S.S. Magnetic and microwave absorbing properties of Co^{2+} substituted nickel–zinc ferrites with the emphasis on initial permeability studies. *J. Magn. Magn. Mater.*, 2016, **401**, P. 938–942.

[14] Kumar R., Kumar H., Singh R.R., Barman P.B. Variation in magnetic and structural properties of Co-doped Ni–Zn ferrite nanoparticles: a different aspect. *J. Sol-Gel Sci. Technol.*, 2016, **78**, P. 566–575.

[15] Bhame S.D., Joy P. Magnetoelastic properties of terbium substituted cobalt ferrite. *Chemical Physics Letters*, 2017, **685**, P. 465–469.

[16] Liu Z., Peng Z., Lv C., Fu X. Doping effect of Sm^{3+} on magnetic and dielectric properties of Ni–Zn ferrites. *Ceram. Int.*, 2017, **43**, P. 1449–1454.

[17] Li L.Z., Zhong X.X., Wang R., Tu X.Q. Structural, magnetic and electrical properties of Zr-substitued NiZnCo ferrite nanopowders. *J. Magn. Magn. Mater.*, 2017, **435**, P. 58–63.

[18] Kabbur S.M., Waghmare S.D., Nadargi D.Y., Sartale S.D., Kambale R.C., Ghodake U.R., et al. Magnetic interactions and electrical properties of Tb^{3+} substituted NiCuZn ferrites. *J. Magn. Magn. Mater.*, 2019, **473**, P. 99–108.

[19] Slimani Y., Almessiere M.A., Güner S., Tashkandi N.A., Baykal A., Sarac M.F., Nawaz M.U., Ercan I. Calcination effect on the magneto-optical properties of vanadium substituted NiFe2O4 nanoferrites. *J. Mater. Sci.: Mater. Electron*, 2019, **30** (10), P. 9143–9154.

[20] Slimani Y., Almessiere M.A., Güner S., Kurtan U., Shirsath S.E., Baykal A., Ercan I. Magnetic and microstructural features of Dy^{3+} substituted $NiFe_2O_4$ nanoparticles derived by sol-gel approach. *J. Sol-Gel Sci. Technol.*, 2020, **95** (1), P. 202–210.

[21] Hua J., Maa Y., Kana X., Liua C., Zhanga X., Rao R., Wanga M., Zheng G. Investigations of Co substitution on the structural and magnetic properties of Ni–Zn spinel ferrite. *J. Magn. Magn. Mater.*, 2020, **513**, 167200.

[22] Devi H.F., Thoithoi Devi K., Singh T.D. Synthesis, characterization, optical and electrical properties of citrate mediated terbium doped ZnO nanoparticles for multifunctional applications. *Integrated Ferroelectrics*, 2020, **204**, P. 81–89.

[23] Deonikar V.G., Kulkarni V.D., Rathod S.M., Kima H. Fabrication and characterizations of structurally engineered lanthanum substituted nickel-cobalt ferrites for the analysis of electric and dielectric properties. *Inorganic Chemistry Communications*, 2020, **119**, 108074.

[24] Skoog D.A., Holler E.J.F., Crouch S.R. *Principles of Instrumental Analysis*. Thomson Books Company Limited, 2007.

[25] Smit J. *Magnetic Properties of Materials*. McGrawHill Book Company, New York, 1971.

Information about the authors:

Shrinivas G. Jamdade – Department of Physics, Nowrosjee Wadia College, Pune, India; ORCID 0000-0002-9393-5619; hv_jamdade@yahoo.com

Popat S. Tambade – Department of Physics, Prof. Ramkrishna More Arts, Commerce and Science College, Akurdi, Pune, India; ORCID 0000-0002-2108-7067; pstam3@rediffmail.com

Sopan M. Rathod – Department of Physics, Abasaheb Garware College, Pune, India; ORCID 0000-0003-2357-9791; smragc@rediffmail.com

Conflict of interest: the authors declare no conflict of interest.